Radiosynthesis and Evaluation of Cyclohexyl (5-(2-[^{11}C-Carbonyl]acetamidobenzo[*d*]thiazol-6-yl)-2-Methylpyridin-3-yl)Carbamate ([^{11}C]PK68) As a New Radioligand For Imaging Receptor-Interacting Protein 1 Kinase

Tomoteru Yamasaki (yamasaki.tomoteru@qst.go.jp)
National Institutes for Quantum and Radiological Science and Technology National Institute of Radiological Sciences: Kokuritsu Kenkyu Kaihatsu Hojin Ryoshi Kagaku Gijutsu Kenkyu Kaihatsu Kiko Hoshasen Igaku Sogo Kenkyujo https://orcid.org/0000-0001-7773-3665

Katsushi Kumata
National Institutes for Quantum and Radiological Science and Technology National Institute of Radiological Sciences: Kokuritsu Kenkyu Kaihatsu Hojin Ryoshi Kagaku Gijutsu Kenkyu Kaihatsu Kiko Hoshasen Igaku Sogo Kenkyujo

Atsuto Hiraishi
National Institutes for Quantum and Radiological Science and Technology National Institute of Radiological Sciences: Kokuritsu Kenkyu Kaihatsu Hojin Ryoshi Kagaku Gijutsu Kenkyu Kaihatsu Kiko Hoshasen Igaku Sogo Kenkyujo

Yiding Zhang
National Institutes for Quantum and Radiological Science and Technology National Institute of Radiological Sciences: Kokuritsu Kenkyu Kaihatsu Hojin Ryoshi Kagaku Gijutsu Kenkyu Kaihatsu Kiko Hoshasen Igaku Sogo Kenkyujo

Hidekatsu Wakizaka
National Institutes for Quantum and Radiological Science and Technology National Institute of Radiological Sciences: Kokuritsu Kenkyu Kaihatsu Hojin Ryoshi Kagaku Gijutsu Kenkyu Kaihatsu Kiko Hoshasen Igaku Sogo Kenkyujo

Yusuke Kurihara
National Institutes for Quantum and Radiological Science and Technology National Institute of Radiological Sciences: Kokuritsu Kenkyu Kaihatsu Hojin Ryoshi Kagaku Gijutsu Kenkyu Kaihatsu Kiko Hoshasen Igaku Sogo Kenkyujo

Nobuki Nengaki
National Institutes for Quantum and Radiological Science and Technology National Institute of Radiological Sciences: Kokuritsu Kenkyu Kaihatsu Hojin Ryoshi Kagaku Gijutsu Kenkyu Kaihatsu Kiko Hoshasen Igaku Sogo Kenkyujo

Ming-Rong Zhang

National Institutes for Quantum and Radiological Science and Technology National Institute of Radiological Sciences: Kokuritsu Kenkyu Kaihatsu Hojin Ryoshi Kagaku Gijutsu Kenkyu Kaihatsu Kiko Hoshasen Igaku Sogo Kenkyujo

Research Article

Keywords: PK68, PET, RIPK1, [11C]acetyl chloride

Posted Date: January 11th, 2022

DOI: https://doi.org/10.21203/rs.3.rs-1201743/v1

Abstract

Background: Receptor-interacting protein 1 kinase (RIPK1) is a key enzyme in the regulation of cellular necroptosis. Recently, cyclohexyl (5-(2-acetamidobenzo[*d*]thiazol-6-yl)-2-methylpyridin-3-yl)carbamate (PK68, **5**) has been developed as a potent inhibitor of RIPK1. Herein, we radiosynthesized [^{11}C]PK68 as a new positron emission tomography (PET) ligand for imaging RIPK1 and evaluated its potential *in vivo*.

Results: We synthesized [^{11}C]PK68 by reacting amine precursor **14** with [^{11}C]acetyl chloride. At the end of synthesis, we obtained [^{11}C]PK68 of 1200–1790 MBq (n = 10) with >99% radiochemical purity and a molar activity of 37–99 GBq/μmol starting from 18–33 GBq of [^{11}C]CO_2. The fully automated synthesis took 30 min from the end of irradiation. In a small-animal PET study, [^{11}C]PK68 was rapidly distributed in the liver and kidneys of healthy mice after injection, and was subsequently cleared from their bodies via hepatobiliary excretion and the intestinal reuptake pathway. Although there was no obvious specific binding of RIPK1 in the PET study, [^{11}C]PK68 demonstrated relatively high stability *in vivo*, and may be used as a lead compound for further candidate development.

Conclusions: In the present study, we successfully radiosynthesized [^{11}C]PK68 and evaluated its potential *in vivo*. We are planning to optimize the chemical structure of [^{11}C]PK68 and conduct further PET studies on it using pathological models.

Background

Receptor-interacting protein 1 kinase (RIPK1) is a key regulator of neuronal death and is involved in apoptosis and necroptosis; it is related to several disorders including neuroinflammation, neurodegeneration, and carcinogenesis (Chan et al. 2019; DeRoo et al. 2020; Yu et al. 2021; Yuan et al. 2019). RIPK1 is a member of the RIP kinase family and contains a Ser/Thr kinase domain N-terminal, an intermediate domain, and a death domain C-terminal (Sunde et al. 1997; Zhang et al. 2018a). The death domain of RIPK1 binds to tumor-necrosis factor-associated proteins related to cellular death. In addition, the intermediate and death domains of RIPK1 enable it to form with a variety of other kinases, such as RIPK3, focal adhesion kinase, and mitogen-activated protein/extracellular signal-regulated kinases (Zhang et al. 2010). Therefore, it is supposed that RIPK1 plays a crucial role in regulating cell death and controlling the homeostasis of tissues and organs.

Several RIPK1 inhibitors have been developed, as shown in Figure 1. Necrostatin-1 (**1**) and its derivative (**2**), which is also called 7-Cl-*O*-Nec-1, were initially identified as allosteric RIPK1 inhibitors (Degterev et al. 2005). However, the half maximal effective concentrations (EC_{50} values) of these compounds were 490 nM for **1** and 210 nM for **2**, which would be insufficient for the positron emission tomography (PET) imaging of RIPK1. Recently, two different types of potent RIPK1 inhibitors have been identified (Figure 1) (Harris et al. 2017; Hou et al. 2019). GlaxoSmithKline (GSK) inhibitors are extremely potent in human cells (IC_{50} = 6.3 nM for **3** and IC_{50} = 10 nM for **4**), and have been used in clinical trials of treatments for inflammatory diseases and central nervous system (CNS) disorders (Weisel et al. 2017; Yuan et al. 2019). However, the efficacy of

these compounds is highly reduced in rodents (IC_{50} >1 μM for **3** and IC_{50} >3 μM for **4**) (Harris et al. 2017; Harris et al. 2019). Although cyclohexyl (5-(2-acetamidobenzo[*d*]thiazol-6-yl)-2-methylpyridin-3-yl)carbamate (PK68, **5**) has lower efficacy than GSK compounds with regard to RIPK1 in human cell lines, it does not exhibit species selectivity (IC_{50} = 23 nM for a human cell line and IC_{50} = 13 nM for a mouse cell line) (Hou et al. 2019).

PET is an advanced molecular imaging modality that is widely used to evaluate distribution *in vivo* and to measure the target occupancy of pharmaceuticals using small animals (Saijo et al. 2009; Yamasaki et al. 2020). Most recently, [^{18}F]CNY-07 ([^{18}F]**6**), an analog of 7-Cl-*O*-Nec-1, has been developed as an initial PET ligand for imaging RIPK1 (Lan et al. 2021) (Figure 2). Although [^{18}F]CNY-07 exhibited relatively high affinity (K_D = 68 nM for RIPK1), its specific binding affinity for RIPK1 *in vivo* was not high. Therefore, to the best of our knowledge no clinically useful PET ligands that can be used to visualize RIPK1 *in vivo* have been developed until now. Herein, we radiolabeled PK68, a potent RIPK1 inhibitor without species selectivity, with ^{11}C via [^{11}C]acetyl chloride ([^{11}C]AcCl), and evaluated its potential as a PET ligand for imaging RIPK1 in mice.

Methods

General

All chemical reagents and organic solvents were purchased from FUJIFILM Wako Pure Chemicals (Osaka, Japan), Tokyo Chemical Industries (Tokyo, Japan), Nacalai Tesque (Kyoto, Japan), and BLD Pharmatech (Shanghai, China), and were used without further purification. Proton nuclear magnetic resonance (^{1}H-NMR) and carbon 13 nuclear magnetic resonance (^{13}C-NMR) spectra were recorded on ECS-400 (JEOL, Tokyo, Japan), ECA-500 (JEOL), and ECZ-600R (JEOL) spectrometers. The chemical shifts of the ^{1}H-NMR and ^{13}C-NMR spectra were reported as δ values (ppm) relative to tetramethyl silane (0 ppm) and relative to $CDCl_3$ (77.0 ppm) or dimethyl sulfoxide (DMSO)-d_6 (39.6 ppm). The splitting patterns were reported as s (singlet); d (doublet); t (triplet); q (quartet); m (multiplet); and br (broad). The coupling constants (J values) are given in hertz (Hz). The electrospray ionization–mass spectrometry (ESI-MS) spectra were recorded on a Q-Exactive Plus spectrometer (Thermo Scientific, Waltham, MA, USA). High-resolution fast atom bombardment mass spectra (HRMS) were acquired using an NMS-SX102 102A spectrometer (JEOL). Column chromatography was performed using Wako-Gel C-200 (100–200 mesh). The purities of the synthesized compounds for biological testing were >98% as determined by analytical high-performance liquid chromatography (HPLC). Unless otherwise stated, radioactivity was measured using an IGC-3R Curiemeter (Hitachi Aloka Medical, Tokyo, Japan). HPLC was performed using a JASCO HPLC system (JASCO, Tokyo, Japan): effluent radioactivity was monitored using a NaI (Tl) scintillation detector system.

Chemical syntheses

6-(4,4,5,5-Tetramethyl-1,3,2-dioxaborolan-2-yl)-2-amino benzo[d]thiazole (8)

A mixture comprising 2-amino-6-bromobenzothiazole (**7**; 2.29 g, 10.0 mmol), bis(pinacolato)diboron (2.79 g, 11.0 mmol), K_2CO_3 (2.94 g, 30 mmol), and Pd(dppf)$_2$ dichloromethane adduct (0.8 g, 1.0 mmol) in 1,4-

dioxane (40 mL) was refluxed under argon for 10 h. The reaction mixture was filtered through a celite bed and washed with AcOEt. After solvent removal, the residue was purified by column chromatography (silica gel, CH_2Cl_2/AcOEt = 100/0 to 80/20) to give **8** as a white powder (2.06 g, 74.6%) with a melting point (mpt) of 218–219°C (recrystallized form *n*-hexane). ^{1}H-NMR (400 MHz, $CDCl_3$) δ 8.06 (1H, s), 7.75 (1H, dd, *J* = 0.9, 9.0 Hz), 7.52 (1H, d, *J* = 8.1 Hz), 5.59 (2H, br), 1.35 (12H, s). ^{13}C-NMR (151 MHz, $CDCl_3$) δ 167.31, 154.47, 132.43, 131.24, 127.70, 118.51, 83.78, 31.57, 24.86. MS (ESI) $[M + H]^+$ calculated for ($C_{19}H_{17}BN_2O_2S$) requires *m/z*, 277.1177; found *m/z*, 277.1170.

2-Acetylamino 6-(4,4,5,5-tetramethyl-1,3,2-dioxaborolan)benzo[d]thiazole (9a)

Acetylchloride (0.4 mL, 6.0 mml) in CH_2Cl_2 (2.0 mL) was added to a mixture comprising **8** (1.10 g, 4.0 mmol), Et_3N (1.39 mL, 10.0 mmol), and *N,N*-dimethylaminopyridine (DMAP) (15 mg, 0.12 mmol) in CH_2Cl_2 (8 mL), which was stirred at room temperature overnight. The reaction was quenched by brine and extracted with CH_2Cl_2. The organic layer was washed with brine, dried over sodium sulfate, and evaporated. The residue was purified by column chromatography (silica gel, *n*-hexane/AcOEt = 90/10 to 80/20) to give **9a** as a white powder (0.96 g, 75.4%) with a mpt of 235–236°C (decomp). ^{1}H-NMR (400 MHz, DMSO–d_6) δ: 12.45 (1H, brs), 8.27 (1H, s), 7.72 (2H, s), 2.21 (3H, s), 1.31 (12H, s). ^{13}C-NMR (125.7 MHz, $CDCl_3$): δ 168.8, 150.0, 149.9, 132.5, 131.4, 128.6, 125.8, 119.6, 83.0, 24.9, 23.5. MS (FAB) $[M + H]^+$ *m/z*, 319.

tert **-Butyl 6-(4,4,5,5-tetramethyl-1,3,2-dioxaborolan-2-yl)benzo[d]thiazol-2-yl-carbamate (9b)**

Di-*tert*-butyl dicarbonate (1.64 g, 7.5 mmol) was added to a mixture comprising **7** (2.0 g. 7.24 mmol), Et_3N (1.39 mL, 10.0 mmol), and DMAP (30 mg, 0.25 mmol) in CH_2Cl_2 (25 mL), which was stirred at room temperature overnight. The reaction mixture was quenched with brine and extracted with CH_2Cl_2. The organic layer was washed with brine, dried over sodium sulfate, and evaporated. The residue was purified by column chromatography (silica gel, *n*-hexane/AcOEt = 90/10 to 80/20) to give **9b** as a white powder (2.17 g, 79.7%) with a mpt >350°C (decomp.) ^{1}H-NMR (400 MHz, $CDCl_3$): δ 11.77 (1H, br), 8.26 (1H, s), 7.91 (1H, d, *J* = 8.1 Hz), 7.82 (1H, dd, *J* = 0.9, 8.1 Hz), 1.60 (9H, s), 1.38 (12H, s). ^{13}C-NMR (151 MHz, $CDCl_3$): δ 163.02, 152.84, 150.97, 131.86, 131.08, 128.00, 120.08, 83.94, 83.39, 28.39, 24.86. HRMS (ESI) $[M + H]^+$ calculated for ($C_{18}H_{26}BN_2O_4S$) requires *m/z*, 377.1701; found *m/z*, 377.1695.

Cyclohexyl 4-nitrophenyl carbonate (11)

A mixture comprising 4-nitrophenyl chloroformate (**10**; 6.05 g, 30.0 mmol), cyclohexanol (3.30 g, 33.0 mmol), and DMAP (0.36 g, 3.0 mmol) in tetrahydrofuran (THF) (15 mL) was stirred at 0°C for 3 h and then at room temperature for 3 h. The reaction mixture was diluted with *n*-hexane and purified by column chromatography (silica gel, *n*-hexane/AcOEt = 95/5) to give **11** as a white powder (3.83 g, 48.1%) with a mpt of 63–64°C. ^{1}H-NMR (400 MHz, $CDCl_3$): δ 8.28 (2H, d, *J* = 9.2 Hz), 7.39 (2H, d, *J* = 9.2 Hz), 4.73–4.80 (1H, m), 1.99–2.05 (2H, m), 1.79–1.84 (2H, m), 1.55–1.64 (4H, m), 1.26–1.47 (2H, m). ^{13}C-NMR (151 MHz, $CDCl_3$): δ 155.66, 151.83, 145.20, 125.23, 121.78, 78.71, 31.33, 25.06, 23.50. MS (FAB) $[M + H]^+$ *m/z*, 266.

Cyclohexyl (5-bromo-2-methylpyridine-3-yl) carbamate (12)

A solution of potassium bis(trimethylsilyl)amide (5.6 mmol) in toluene (0.5 M, 11.2 mL) was added slowly to the mixture of 2-methyl-3-amino-5-bromopyridine (0.5 g, 2.67 mmol) in dry THF (5 mL) at 0°C. After stirring for 15 min at 0°C, a solution of **11** (0.85 g, 3.2 mmol) in THF (5 mL) was added slowly to the mixture described above. The reaction mixture was stirred for 30 min at 0°C. The mixture was quenched with brine and extracted with AcOEt. The organic layer was washed with brine, dried over $MgSO_4$, and then evaporated. The residue was purified by column chromatography on silica gel (*n*-hexane/AcOEt = 90/10 to 80/20) to give **12** as a pale-yellow powder (0.63 g, 75.7%) with a mpt of 95–96°C. ^{1}H-NMR (400 MHz, $CDCl_3$): δ 8.48 (1H, br), 8.26 (1H, d, *J* = 2.0 Hz), 6.43 (1H, s), 4.76 (1H, m), 2.46 (3H, s), 1.74-1.97 (4H, m), 1.22–1.60 (6H, m). ^{13}C-NMR (151 MHz, $CDCl_3$): δ 152.82, 144.25, 133.67, 129.02, 118.30, 115.63, 74.74, 31.82, 25.24, 23.78, 20.26. MS (FAB) $[M + H]^+$ *m/z*, 313.

Cyclohexyl 5-(2-acetylamino-benzo[d]thiazol-6-yl)-2-methylpyridin-3-ylcarbamate (PK68, 5)

A mixture comprising 12 (478 mg, 1.5 mmol), 9a (376 mg, 1.0 mmol), K_2CO_3 (520 mg, 3.75 mmol), and $Pd(Ph_3P)_4$ (173 mg, 0.15 mmol) in 1,4-dioxane/H_2O (15 mL/3 mL) was refluxed under argon for 12 h. The reaction mixture was filtered through a celite bed and washed with AcOEt. The crude product was extracted with AcOEt, and the organic layer was washed with brine and dried over $MgSO_4$, then evaporated. The residue was purified by column chromatography on silica gel (CH_2Cl_2/CH_3OH = 100/0 to 90/10) to give PK68 (5) as a pale-yellow powder (440 mg, 69.1%) with a mpt >350 °C (decomp). ^{1}H-NMR (400 MHz, DMSO–d_6): δ 9.14 (1H, s), 8.59 (1H, d, *J* = 2.0 Hz), 8.30 (1H, d, *J* = 1.6 Hz), 8.10 (1H, d, *J* = 1.8 Hz), 7.81 (1H, d, *J* = 8.5 Hz), 7.71 (1H, dd, *J* =1.9, 8.4 Hz), 4.62–4.68 (1H, m), 3.45 (1H, br), 2.46 (3H, s), 2.21 (3H, s), 1.91–1.94 (2H, m), 1.71–1.74 (2H, m), 1.21–1.52 (6H, m). ^{13}C-NMR (125.7 MHz, DMSO–d_6): δ 169.5, 158.6, 154.0, 150.3, 148.4, 142.6, 133.3, 132.9, 132.6, 132.2, 129.0, 120.9, 119.7, 72.9, 31.6, 24.9, 23.5, 22.8, 20.7. HRMS (FAB) $[M + H]^+$ calculated for ($C_{22}H_{25}N_4O_3S$) requires *m/z*, 425.1647; found *m/z*, 425.1652.

Cyclohexyl 5-(2-tert-butoxycarbonyl-aminobenzo[d]thiazol-6-yl)-2-methylpyridin-3-ylcarbamate (13)

A mixture comprising **12** (313 mg, 1.0 mmol), **9b** (376 mg, 1.0 mmol), K_2CO_3 (210 mg, 1.5 mmol), and $Pd(Ph_3P)_4$ (116 mg, 0.1 mmol) in 1,4-dioxane/H_2O (10 mL/2 mL) was refluxed under argon for 12 h. The reaction mixture was filtered through a celite bed and washed with AcOEt. The crude product was extracted with AcOEt and the organic layer was washed with brine, dried over $MgSO_4$, and then evaporated. The residue was purified by column chromatography on silica gel (CH_2Cl_2/CH_3OH = 100/0 to 90/10) to give **13** as a pale-yellow powder (206 mg, 42.7%) with a mpt >350°C (decomp). ^{1}H-NMR (400 MHz, DMSO–d_6): δ 11.87 (1H, br), 9.14 (1H, s), 8.59 (1H, d, *J* = 2.0 Hz), 8.28 (1H, d, *J* = 1.8 Hz), 8.10 (1H, s), 7.76 (1H, d, *J* = 8.3 Hz), 7.69 (1H, d, *J* = 10.1 Hz), 4.62–4.68 (1H, m), 2.46 (3H, s), 1.91–1.99 (2H, m), 1.72–1.74 (2H, m), 1.53 (9H, s), 1.29–1.45 (6H, m). ^{13}C-NMR (151 MHz, DMSO–d_6) δ: 160.2, 153.6, 150.2, 149.2, 142.6, 133.3, 132.9, 132.6, 131.8, 131.5, 128.8, 124.8, 120.6, 119.5, 81.8, 72.6, 31.6, 27.9, 24.9, 23.4, 20.7. HRMS (ESI) $[M + H]^+$ calculated for ($C_{25}H_{31}N_4O_4S$) requires *m/z*, 483.2066 ; found *m/z*, 483.2055.

Cyclohexyl-5-(2-aminobenzo[d **]thiazol-6-yl)-2-methylpyridin-3-ylcarbamate (14)**

A mixture comprising **13** (100 mg, 0.21 mmol in CH_3OH (10 mL) and 2 mol/L HCl (5 mL) was stirred at 60°C overnight. Et_3N (1.5 mL) was added to the reaction mixture and evaporated. The crude product was washed with water and purified by column chromatography (silica gel CH_2Cl_2/CH_3OH = 100/0 to 97/3) to give **14** as a white powder (44.3 mg, 55.1%) with a mpt >350°C (decomp). ^{1}H-NMR (400 MHz, DMSO–d_6): δ 9.10 (1H, s), 8.53 (1H, d, *J* = 1.8 Hz), 8.02 (2H, d, *J* = 11.9 Hz), 7.61 (2H, br), 7.51 (1H, dd, *J* = 1.5, 8.2 Hz), 7.41 (1H, d, *J* = 8.3 Hz), 4.61–4.67 (1H, m), 2.44 (3H, s), 1.90–1.93 (2H, m), 1.72–1.77 (2H, m), 1.16–1.48 (6H, m). ^{13}C-NMR (151 MHz, DMSO-d_6): δ 167.14, 153.93, 152.78, 149.68, 142.26, 133.51, 132.77, 132.09, 129.46, 124.16, 118.92, 118.01, 72.78, 40.03, 24.88, 23.42, 20.64. HRMS (ESI) $[M + H]^+$ calculated for $C_{20}H_{22}N_4O_2S$) requires *m/z*, 383.1542; found *m/z*, 383.1531.

Radiochemistry

Cyclohexyl (5-(2-[^{11}C-carbonyl]acetamidobenzo[d]thiazol-6-yl)-2-methylpyridin-3-yl)carbamate ([^{11}C]PK68)

^{11}C was produced by the ^{14}N (p, α)^{11}C nuclear reaction using a CYPRIS HM-18 cyclotron (Sumitomo Heavy Industry, Tokyo, Japan). An automated multi-purpose synthesizer developed in-house (Fukumura et al. 2007) was used for all radiosynthetic runs in the present study.

[^{11}C]Acetyl chloride ([^{11}C]AcCl) was produced according to our previous procedure (Arai et al. 2009). Briefly, no-carrier-added [^{11}C]CO_2 was produced by the bombardment of dry N_2 gas (1.5 MPa; Nippon Sanso, Japan) containing 0.01% O_2 (Nippon Sanso) with a beam (15 mA) of 18 MeV protons. During the production of [^{11}C]CO_2, a solution of CH_3MgBr (1.0 mol/L in THF, 500 mL) was loaded on the surface of a polyethylene loop, which was flushed with N_2 to remove excess CH_3MgBr solution.

After irradiation, [^{11}C]CO_2 was carried from the target with a N_2 stream and trapped in a stainless-steel coil cooled to between −170°C and −165°C. The coil was warmed to 50°C with hot air, and the concentrated [^{11}C]CO_2 was transferred to a cooled loop coated with the CH_3MgBr solution until the level of radioactivity trapped in the loop reached a plateau. The radioactive mixture was transferred to the reaction vessel by passing oxalyl chloride $(COCl)_2$/THF (10/400, 400 mL) through the loop, and heated at 50°C for 2 min to produce [^{11}C]AcCl.

The [^{11}C]AcCl in the reaction vessel was distilled and trapped in a solution of **14** (1.0 mg), Et_3N (5 mL), and DMAP (1 mg) in dry THF (300 mL). The reaction mixture was heated at 80°C for 5 min. After the reaction, the reaction mixture was transferred to the injector for semipreparative HPLC. The preparative HPLC conditions were as follows: Triart C18 column (5 μm, 10 mm i.d. × 250 mm length, YMC), CH_3CN/H_2O/trifluoroacetic acid (TFA) (40/60/0.1%) as a mobile phase, a flow rate of 5.0 mL/min, and UV detection at 254 nm. The retention time (t_R) of [^{11}C]PK68 was approximately 7.5 min. The HPLC fraction of [^{11}C]PK68 was collected in a flask to which polysorbate 80 (75 μL) in ethanol (0.3 mL) and ascorbic acid (25 mg/0.1 mL by injection) had been added before radiosynthesis. The solution was subsequently evaporated to dryness, and the

residue was dissolved in physiological saline (5 mL). The resulting solution was passed through a Millex-GV filter (Millipore) to obtain [^{11}C]PK68 as an injectable solution.

Radiochemical purity, identification, and molar activity were measured by analytical HPLC [mobile phase: CH_3CN/H_2O/TFA = 45/55/0.1%; flow rate: 1.0 mL/min; UV absorbance: 254 nm] using a Triart C18 column (4.6 mm i.d. × 250 mm length, YMC). The t_R was 5.0 min for [^{11}C]PK68. The identification of [^{11}C]PK68 was confirmed by co-injection with the corresponding unlabeled PK68. The mass (μmol) of [^{11}C]PK68 with a known radioactivity (GBq) was determined by analytical HPLC comparison of the UV absorbance at 254 nm of [^{11}C]PK68 with that of known concentrations of unlabeled PK68.

Lipophilicity of [^{11}C]PK68

The logD value was measured by mixing [^{11}C]PK68 with n-octanol (3.0 g) and phosphate-buffered saline (PBS; 3.0 g, 0.1 M, pH 7.4) in a test tube, which was vortexed for 3 min at room temperature, then centrifuged at 3500 *g* for 5 min. An aliquot of 0.65 mL PBS and 0.65 mL n-octanol was removed and weighed, and its radioactivity was determined using an autogamma counter (2480 Wizard^2, Perkin-Elmer, Waltham, MA, USA). Each sample from the remaining organic layer was removed and repartitioned until a consistent logD value was obtained. The logD value was calculated by comparing the ratio of counts per minute (cpm)/g of n-octanol to that of PBS, and is expressed as logD = log[cpm/g (n-octanol)/cpm/g (PBS)]. All measurements were performed in triplicate.

Animal experiments

Animals

Male ddY mice were purchased from Japan SLC (Shizuoka, Japan), kept in a temperature-controlled environment under a 12 h light–dark cycle, and fed a standard diet (MB-1; Funabashi Farm, Chiba, Japan). The animal experiments were conducted according to the recommendations made by the Committee for the Care and Use of Laboratory Animals at the National Institutes for Quantum Science and Technology, and were approved by the Committee of National Institutes for Quantum Science and Technology (approval number: 16-1006).

Small-animal PET imaging

Each mouse was anesthetized using 1.5% (v/v) isoflurane, and an intravenous catheter was inserted into its tail vein. The mice (10–14 weeks old, 48.1 ± 7.4 g) were subsequently maintained under anesthesia and secured in a custom-designed chamber placed in the center of a small-animal PET scanner (Inveon, Siemens Healthineers, Erlangen, Germany). After adjusting the target position for scanning, dynamic emission scans (in three-dimensional list mode) were performed for 60 min (1 min × 4 frames, 2 min × 8 frames, and 5 min × 8 frames). [^{11}C]PK68 (11–16 MBq) was injected via a tail vein catheter. The body temperature of each mouse was maintained at 37°C using a heated (40°C) water circulation system (T/Pump TP401, Gaymar Industries, NY, USA) during the PET scan. For the blocking study, the mice were pre-dosed with unlabeled PK68 (1 mg/kg) before the injection of [^{11}C]PK68. The obtained dynamic PET images (0.6 mm slice

thickness) were reconstructed by filtered-back projection using a Hanning filter, with a Nyquist cutoff of 0.5 cycles per pixel. The time–activity curves (TACs) of [^{11}C]PK68 were acquired using PMOD software (version 3.4, PMOD Technology, Zurich, Switzerland) from the volumes of interest, which were manually mapped onto the heart, lung, liver, kidney, muscle, and brain. The radioactivity was decay-corrected to the injection time and is expressed as a standardized uptake value (SUV), normalized for injected radioactivity and body weight,. The SUV was calculated according to the following formula: SUV = (radioactivity per milliliter tissue/injected radioactivity) × body weight (g). We also calculated the area under the curve (AUC) using TACs from 0 to 60 min.

Metabolite analysis

Following intravenous injection of [^{11}C]PK68 (37 MBq, 0.1 mL), the mice (8–9 weeks, 40.1 ± 5.3 g) were killed by cervical dislocation at 5, 15, 30, and 60 min. Blood and liver samples were obtained immediately. Each blood sample was centrifuged in a heparinized tube at 15,000 *g* for 2 min at 4°C to separate the plasma. The supernatant was collected in a test tube containing CH_3CN, and the resulting mixture was vortexed for 15 s, then centrifuged at 15,000 *g* for 2 min for deproteinization. The resulting supernatant was collected. Each liver sample was homogenized using a Silent Crusher S homogenizer (Rose scientific, Edmonton, Canada) in ice-cooled saline. The resulting homogenate was mixed with an equivalent amount of CH_3CN, and centrifuged at 15,000 *g* for 2 min for deproteinization. An aliquot of the supernatant (0.1–1.0 mL) obtained from the plasma or liver homogenate was injected into the HPLC system with a radioactivity detector, and analyzed using a Capcell Pak C_{18} column (4.6 mm i.d. × 250 mm, Shiseido) with a mobile phase [CH_3CN/H_2O/TFA, (45/55/0.1, v/v/v)] at a flow rate of 1.0 mL/min. The percentage ratio of [^{11}C]PK68 (t_R = 5.0 min) to total radioactivity (corrected for decay) on the HPLC chromatogram was calculated as % = (peak area for [^{11}C]PK68/total peak area) × 100.

Ex vivo biodistribution study

Each mouse (8 weeks old, 37.9 ± 1.0 g) was injected with a bolus of [^{11}C]PK68 (2.7 MBq, 0.1 mL) via its tail vein. Three mice were sacrificed by cervical dislocation at each experimental time-point (1, 5, 15, 30, and 60 min) after the injection. The blood (heart contents), heart wall, lung, liver, pancreas, spleen, kidneys, adrenals, stomach (including contents), small intestine (including contents), large intestines (including contents), testes, muscles, and whole brain were removed quickly and weighed. The radioactivity in these tissues was measured with an autogamma scintillation counter (2480 Wizard^2, Perkin-Elmer, MA, USA) and expressed as %ID/g. All radioactivity measurements were corrected for decay.

Statistical analysis

Data are expressed as the mean ± standard deviation. Comparisons were made using two-way analysis of variance (ANOVA) with the Bonferroni post hoc test. The analysis was performed using GraphPad Prism 5 software (GraphPad Software, CA, USA). Differences between groups were considered significant when $P < 0.05$.

Results

Chemistry

The standard sample PK68 and its ^{11}C-labeling precursor **14** were obtained following the synthetic routes shown in Scheme 1. The procedures were performed according to the method described in the literature (Zhang et al, 2018b) with some modifications. The reaction of **8** with the corresponding acylating agents gave the intermediate amides **9a** and **9b** in 75% and 80% yields, respectively. Another carbamate intermediate **12** was obtained through the amidation of bicarbonate **11** with 2-methyl-3-amino-5-bromopyridine in 76% yield. PK68 and a *tert*-butoxycarbonyl (BOC) group-protecting intermediate **13** were obtained via a palladium-catalyzed cross-coupling reaction between **9a** or **9b** and **12** in 69% and 43% yields, respectively. The treatment of 2 mol/L HCl converted **13** to the ^{11}C-labeling precursor **14** in 55% yield.

Radiochemistry

Starting from 18–33 GBq of [^{11}C]CO_2, we prepared 1200–1790 GBq of [^{11}C]PK68 with a radiochemical yield of 9.1 ± 5.9% (n = 10) (decay-corrected to the end of irradiation). The identity of [^{11}C]PK68 was determined by HPLC analysis based on the co-injection of this radioactive product with non-radioactive PK68. The radiochemical purity of the [^{11}C]PK68 solution was determined to be greater than 99%, with molar activity of 37–99 GBq/μmol. The radiochemical purity of [^{11}C]PK68 remained greater than 95% after standing for 90 min at room temperature, indicating that this product was radiochemically stable for the period required for at least one PET scan. The lipophilicity (logD) of [^{11}C]PK68 was 4.0, which was slightly over the range of moderate lipophilicity (2–3.5) for a PET ligand (Pike 2009).

Small-animal PET imaging using mice

To evaluate the *in vivo* kinetic and specific uptake of [^{11}C]PK68, dynamic PET scans were conducted using mice treated with or without unlabeled PK68 at a concentration of 1 mg/kg. Figure 3 shows representative dynamic (0–5, 5–15, 15–30, and 30–60 min) and summed (0–60 min) PET images of the baseline (A) and self-blocking (B) mice (n = 2 in each group). In baseline mouse (A), the highest uptake of radioactivity in the early phase (0–5 min) was observed in the liver, followed by the kidneys. These uptakes of radioactivity declined with time, whereas radioactivity in the intestine increased in the late phase (>30 min). The uptake of radioactivity by the other organs was low. Notably, the uptake of radioactivity by the brain was extremely low (<0.3 SUV). Following co-administration with unlabeled PK68, the radioactivity signals in the liver and kidney decreased slightly in the initial phase (~15 min), suggesting specific binding to RIPK1 (Fig. 3B).

Figure 4 shows TACs of [^{11}C]PK68 in the baseline (A) and self-blocking (B) mice and AUCs of radioactivity in the regions of interest (C). The radioactivity values in the liver and kidneys peaked at 2.5 and 1.5 min after injection, and were 4.8 SUV and 2.7 SUV, respectively. By self-blocking, these radioactivity values declined to 4.2 SUV for the liver and 2.3 SUV for the kidneys. Although self-blocking reduced the maximum SUV values in the liver and kidneys by 11% and 15%, respectively, there were no significant differences in the AUC values in these tissues between the groups.

Metabolite analysis

To investigate the metabolic stability of [^{11}C]PK68 *in vivo*, we conducted metabolite analysis using plasma and liver samples removed from mice (n = 2 at each time-point). Figure 5 shows the percentages of unchanged [^{11}C]PK68 in the plasma and liver. The fraction corresponding to [^{11}C]PK68 (t_R = 5.0 min) in the plasma gradually decreased to 85% at 5 min, 66% at 15 min, 65% at 30 min, and 57% at 60 min after injection. A polar radiolabeled metabolite (t_R = 1.5 min) was observed in the plasma samples analyzed by HPLC (data not shown). Similarly, the levels of the unchanged form of [^{11}C]PK68 in the liver were 85% at 5 min, 67% at 15 min, 68% at 30 min, and 57% at 60 min.

Biodistribution of [^{11}C]PK68 in the mice

To evaluate the distribution of [^{11}C]PK68 in peripheral tissues, we performed *ex vivo* biodistribution study using mice. The radioactive concentrations (%ID/g tissue) of [^{11}C]PK68 at various time-points (e.g., 1, 5, 15, 30, and 60 min) in each mouse tissue are shown in Table 1. At 1 min after injection of the radioligand, there was high uptake (>5%ID/g) by the heart, lungs, liver, kidneys, and adrenals, which, with the exception of the liver, demonstrated the washout times from those organs. In the liver, the radioactivity decreased rapidly following an intense increment at 5 min after injection. However, the radioactivity in the small intestine increased with time, and reached a maximum level (>25%ID/g) 60 min after injection.

Table 1

Biodistribution of [^{11}C]PK68 in mice (n = 3, mean ± SD). Radioactivity is expressed as %ID/g.

Tissue	Time after the injection (min)														
	1			5			15			30			60		
Blood	2.4	±	0.3	1.3	±	0.2	1.1	±	0.1	0.8	±	0.1	0.5	±	0.1
Heart	7.6	±	0.3	2.8	±	0.3	2.1	±	0.3	1.3	±	0.1	0.7	±	0.1
Lung	5.2	±	0.2	2.6	±	0.2	2.1	±	0.3	1.5	±	0.2	0.8	±	0.1
Liver	8.0	±	0.8	17.2	±	0.7	15.6	±	0.8	10.7	±	0.3	6.0	±	0.2
Pancreas	3.4	±	0.2	2.7	±	0.3	2.1	±	0.3	1.4	±	0.1	0.8	±	0.1
Spleen	1.5	±	0.2	1.6	±	0.1	1.4	±	0.2	0.9	±	0.0	0.5	±	0.1
Kidney	10.3	±	0.5	9.9	±	0.4	7.7	±	1.0	6.2	±	0.6	3.2	±	0.1
Adrenals	6.2	±	2.7	4.0	±	0.5	3.3	±	0.5	2.1	±	0.8	1.2	±	0.1
Stomach	1.2	±	0.2	2.0	±	0.1	4.0	±	1.2	4.7	±	1.0	7.2	±	2.4
Small intestine	1.8	±	0.1	3.3	±	0.1	9.8	±	3.1	16.7	±	1.4	27.7	±	3.0
Large intestine	0.7	±	0.1	0.9	±	0.1	1.4	±	0.3	1.7	±	0.4	2.6	±	0.6
Testis	0.3	±	0.1	0.3	±	0.0	0.3	±	0.0	0.3	±	0.0	0.2	±	0.0
Muscle	1.9	±	0.3	1.1	±	0.1	0.8	±	0.1	0.6	±	0.1	0.3	±	0.0
Brain	0.6	±	0.0	0.4	±	0.0	0.3	±	0.0	0.2	±	0.0	0.1	±	0.0

Discussion

RIPK1 is an attractive target for the development of pharmaceuticals for the treatment of several CNS disorders, cancers, and cardiovascular disease. PET imaging enables noninvasive evaluations of drug dynamics and estimations of drug occupancy for target molecule *in vivo*. Most recently, RIPK1 imaging in the brain has been conducted using [^{18}F]CNY-07 (Figure 2), an initial PET ligand for RIPK1 (Lan et al, 2021). The radioactive uptake of [^{18}F]CNY-07 was very high (3%ID/cc) in the whole brains of healthy mice, and remained at high levels during the PET scan. Although the specific binding of [^{18}F]CNY-07 for RIPK1 was slight owing to self-blocking, brain uptake of radioactivity might almost correspond to nonspecific or off-target binding, but not to RIPK1 binding. Therefore, to the best of our knowledge, until now there has been no useful PET ligand for imaging RIPK1.

In the present study, we selected PK68 (**5**) as the candidate PET imaging agent for RIPK1. PK68 has recently been identified as a potent inhibitor of RIPK1. It has high affinity for RIPK1 and exerts a strong inhibitory effect on it in human and mouse tumor cells (Hou et al. 2019). Furthermore, tumor-bearing mice treated with

PK68 exhibit a significant reduction in the number of tumor metastases that is the same as in tumor-bearing mice treated with Necrostatin-1. As mentioned above, PK68 is a promising candidate with a sufficient profile as a novel PET ligand (Hou et al. 2019).

We initially decided to label PK68, which has an unsymmetrical urea moiety, using [^{11}C]phosgene (Ogawa et al. 2010). However, we failed to obtain [^{11}C]PK68 and found that symmetrical cyclohexyl [^{11}C]bicarbonate was a major product. We then labeled PK68 using [^{11}C]AcCl, and successfully obtained [^{11}C]PK68 with enough radioactivity for an animal evaluation study (Scheme 2). The [^{11}C]PK68 solution maintained 95% radiochemical purity after 90 min at room temperature, indicating it would be radiochemically stable for the duration of one PET scan.

In PET imaging using mice, the brain uptake of [^{11}C]PK68 was unfortunately inferior to that of [^{18}F]CNY-07, and the maximum uptake in the brain was under 0.25 SUV (<1%ID/cc) (Figures 3A and 4A). It has been suggested that, to some extent, the permeability of the brain with regard to [^{11}C]PK68 may be restricted by ATP-binding cassette transporters at the brain–blood barrier. Or, [^{11}C]PK68 might readily bind to plasma protein owing to its high lipophilicity, impeding entry into the brain. More importantly, the low uptake of [^{11}C]PK68 by the brain demonstrated moderate clearance, which decreased by under 0.1 SUV by the end of the PET scan. This contrasted with [^{18}F]CNY-07, and meant that [^{11}C]PK68 had little nonspecific or off-target binding affinity. Although PET using [^{11}C]PK68 was unable to detect specific RIPK1 binding in the brains of healthy mice, the low nonspecific binding of [^{11}C]PK68 may be favorable for the visualization of RIPK1 when pathological models of the CNS that induce RIPK1 upregulation are used.

RIPK1 is constitutively expressed both in the brain and in many peripheral organs (Zhang et al. 2010). Herein, we evaluated the dynamics of [^{11}C]PK68 in the peripheral organs *in vivo*. In the PET imaging and biodistribution studies on healthy mice, [^{11}C]PK68 rapidly accumulated in the liver and kidneys, and subsequently its radioactive metabolites were distributed in the small intestine (Figure 3A and Table 1). Such dynamics indicate typical hepatobiliary excretion and the intestinal reuptake pathway, which dominates the whole-body distribution of radioactivity and rapid washout from the body after injection. In this manner, we successfully demonstrated the biodistribution of PK68 in mice by PET imaging and dissection. This will improve our understanding of the kinetics of PK68 derivatives for the further development of PET ligand candidates for imaging RIPK1. To confirm the specific binding of [^{11}C]PK68 for RIPK1 in the peripheral organs, we also performed a blocking study by co-administering unlabeled PK68 (1 mg/kg). As shown in the PET images, radioactive uptake in the liver was reduced by self-blocking in the initial phase (0–5 min) after the injection (Figure 3A). Although the differences between the control and self-blocking subjects with regard to the AUC values of the liver were insignificant (Figure 4C), a slight reduction in radioactive uptake by the liver owing to self-blocking might have corresponded with the specific binding of [^{11}C]PK68 with RIPK1. The metabolite analysis revealed that the level of the unchanged form of [^{11}C]PK68 was slightly higher in the liver than in the plasma until 30 min after the injection (Figure 5). These results indicate that radioactive uptake by the liver may involve the specific binding of [^{11}C]PK68 with RIPK1. Interestingly, the metabolite rate of [^{11}C]PK68 in the plasma were relatively slow, and the level of the

unchanged form of [^{11}C]PK68 remained >50% 60 min after the injection. *In vivo*, [^{11}C]PK68 labeled with the [^{11}C]acetyl group would be more stable than the useful PET ligands labeled with the [^{11}C]methyl group (Bertoglio et al. 2020; Kida et al. 2003; Schou et al. 2009; Yanamoto et al. 2009). This indicates that [^{11}C]PK68 has a favorable profile as a PET ligand for imaging target molecules. Therefore, [^{11}C]PK68 may enable the visualization of upregulated RIPK1 under pathological conditions, even though the current work using healthy animals did not reveal significant specific binding to RIPK1. Moreover, [^{11}C]PK68 would be a useful lead compound for the further development of PET ligand candidates.

Conclusions

In the present study, we successfully synthesized [^{11}C]PK68 as a PET ligand for imaging RIPK1. However, PET imaging revealed no specific affinity of [^{11}C]PK68 for RIPK1 in healthy mice. Because the *in vivo* stability of [^{11}C]PK68 is high (> 50% after 60 min in the plasma), it may enable the visualization of RIPK1 if an inflammation model is used. In future experiments, we will investigate the specific binding of RIPK1 in PET studies using pathological animal models, such as neuroinflammation, ischemia, and tumor-bearing models. We will also optimize the chemical structures of promising candidates for imaging RIPK1.

Abbreviations

[^{11}C]AcCl: [^{11}C]acetyl chloride; AUC: area under the curve; CNS: central nervous system; ESI-MS: electrospray ionization–mass spectrometry; PK68: cyclohexyl (5-(2-acetamidobenzo[*d*]thiazol-6-yl)-2-methylpyridin-3-yl) carbamate; mpt: melting point; HRMS: high-resolution fast atom bombardment mass spectra; %ID/g: percentage of injection dose per gram tissue; PET: positron emission tomography; RIPK1: receptor-interacting protein 1 kinase; t_R: retention time; SUV: standardized uptake value; TMS: tetramethylsilane; TAC: time-activity curve; TFA: trifluoroacetic acid.

Declarations

Ethics approval and consent to participate

The animal experiments were conducted according to the recommendations made by the Committee for the Care and Use of Laboratory Animals at the National Institutes for Quantum Science and Technology, and were approved by the Committee of National Institutes for Quantum Science and Technology (approval number: 16-1006).

Consent for publication

Not applicable.

Availability of data and materials

Data can be obtained upon request.

Competing interests

The authors declare that they have no competing interests.

Funding

This work was supported a Grant-in-Aid for Scientific Research (number B-20H03635) from the Japanese Ministry of Education, Culture, Sports, Science, and Technology, and by the Moonshot Research and Development Program (grant number 21zf0127003h001) from the Japan Agency for Medical Research and Development.

Authors' contributions

TY performed the animal experiments and was a major contributor to the writing of the manuscript. KK contributed to the chemical and radiochemical syntheses. AH supported the animal experiments and analyzed the biodistribution data. YZ supported the animal experiments. HW operated the PET scanner. NN supported the radiosynthesis. MZ designed the study and edited the manuscript. All the authors have read and approved the final manuscript.

Acknowledgments

We thank Frank Kitching, MSc., from Edanz (https://jp.edanz.com/ac) for editing a draft of this manuscript. We would also like to thank the staff at the National Institutes for Quantum Science and Technology for their support with the cyclotron and radionuclide production, and the staff at the Center for Analytical Instrumentation of Chiba University for their technical support with the NMR operation.

References

1. Arai T, Zhang MR, Ogawa M, Fukumura T, Kato K, Suzuki K. Efficient and reproducible synthesis of [1-11C]acetyl chloride using the loop method. Appl Radiat Isot. 2009;67(2):296–300.
2. Bertoglio D, Verhaeghe J, Korat S, Miranda A, Wyffels L, Stroobants S, Mrzljak L, Dominguez C, Liu L, Skinbjerg M, Munoz-Sanjuan I, Staelens S. Mol Imaging Biol. 2020;22(4):854–863.
3. Chan HH, Koh RY, Lim CL, Leong CO. Receptor-interacting protein kinase 1 (RIPK1) as a potential therapeutic target: an overview of its possible role in the pahtogenesis of Alzheimer's disease. Curr Alzheimer Res. 2019;16(10):907–918.
4. Degterev A, Huang Z, Boyce M, Li Y, Jagtap P, Mizushima N, Cuny GD, Mitchison TJ, Moskowitz MA, Yuang J. Chemical inhibitor of nonapoptotic cell death with therapeutic potential for ischemic brain injury. Nat Chem Biol. 2005;1(2):112–119.
5. DeRoo E, Zhou T, Liu B. The role of RIPK1 and RIPK3 in cardiovascular disease. Int J Mol Sci. 2020;21(21):8174.
6. Fukumura T, Suzuki H, Mukai K, Zhang MR, Yoshida Y, Nemoto K, Suzuki K. Development of versatile synthesis equipment for multiple production of PET radiopharmaceuticals. J Label Compd Radiopharm. 2007;50(1):S202.

7. Harris PA, Berger SB, Jeong JU, Nagilla R, Bandyopadhyay D, Campobasso N, Capriotti CA, Cox JA, Dare L, Dong X, Eidam PM, Finger JN, Hoffman SJ, Kang J, Kasparcova V, King BW, Lehr R, Lan Y, Leister LK, Lich JD, MacDonald TT, Miller NA, Ouellette MT, Pao CS, Rahman A, Reilly MA, Rendina AR, Rivera EJ, Schaeffer MC, Sehon CA, Singhaus RR, Sun HH, Swift BA, Totoritis RD, Vossenkämper A, Ward P, Wisnoski DD, Zhang D, Marquis RW, Gough PJ, BertinBan J. Discovery of a First-in-Class Receptor Interacting Protein 1 (RIP1) Kinase Specific Clinical Candidate (GSK2982772) for the Treatment of Inflammatory Diseases. J Med Chem. 2017;60(4):1247–1261.
8. Harris PA, Marinis JM, Lich JD, Berger SB, Chirala A, Cox JA, Eidam PM, Finger JN, Gough PJ, Jeoug JU, Kang J, Kasparcova V, Leister LK, Mahajan MK, Miller G, Nagilla R, Ouellette MT, Reilly MA, Rendina AR, Rivera EJ, Sun HH, Thorpe JH, Totoritis RD, Wang W, Wu D, Zhang D, Bertin J, Marquis RW. Identification of a RIP1 Kinase Inhibitor Clinical Candidate (GSK3145095) for the Treatment of Pancreatic Cancer. ACS Med Chem Lett. 2019;10(6):857–862.
9. Hou J, Ju J, Zhang Z, Zhao C, Li Z, Zheng J, Sheng T, Zhang H, Hu L, Yu X, Zhang W, Li Y, Wu M, Ma H, Zhang X, He S. Discovery of potent necroptosis inhibitors targeting RIPK1 kinase activity for the treatment of inflammatory disorder and cancer metastasis. Cell Death Dis. 2019;10(7):493.
10. Kida T, Noguchi J, Zhang MR, Suhara T, Suzuki K. Metabolite analysis of [11C]Ro15-4513 in mice, rats, monkeys, and humans. Nucl Med Biol. 2003;30:779–784.
11. Lan Y, Bai P, Afshar S, Striar R, Rattray AK, Meyer TN, Langan AG, Posner AM, Shen S, Tanzi RE, Zhang C Wang C. Visualization of receptor-interacting protein kinase 1 (RIPK1) by brain imaging with positron emission tomography. 2021;64:15420–15428.
12. Ogawa M, Takada Y, Suzuki H, Nemoto K, Fukumura T. Simple and effective method for producing [11C]phosgene using an environmental CCl4 gas detection tube. Nucl Med Biol. 2010;37(1):73–76.
13. Pike VW. PET radiotracers: crossing the blood-brain barrier and surviving metabolism. Trends Pharmacol Sci. 2009;30:431–440.
14. Saijo T, Maeda J, Okauchi T, Maeda J, Morio Y, Kuwahara Y, Suzuki M, Goto N, Suzuki K, Higuchi M, Suhara T. Utility of small-animal positron emission tomographic imaging of rats for preclinical development of drugs acting on the serotonin transporter. Int J Neuropsychopharmacol. 2009;12(8):1021–1032.
15. Schou M, Zoghbi SS, Shetty HU, Shchukin E, Liow JS, Hong J, Andree BA, Gulyas B, Farde L, Innis RB, Pike VW, Halldin C. Investigation of the metabolites of (S,S)-[11C]MeNER in humans, monkeys and rats. Mol Imaging Biol. 2009;11(1):23–30.
16. Sunde M, Serpell LC, Bartlam M, Fraser PE, Pepys MB, Blake CC. J Mol Biol. 1997;273(3):729–739.
17. Weisel K, Scott NE, Tompson DJ, Votta BJ, Madhavan S, Povey K, Wolstenholme A, Simeoni M, Rudo T, Richards-Peterson L, Sahota T, Wang JG, Lich J, Finger J, Verticelli A, Reilly M, Gough PJ, Harris PA, Bertin J, Wang ML. Randomized clinical study of safety, pharmacokinetics, and pharmacodynamics of RIPK1 inhibitor GSK2982772 in healthy volunteers. Pharmacol Res Perspect. 2017;5(6):e00365.
18. Yamasaki T, Ohya T, Mori W, Zhang Y, Wakizaka H, Nengaki N, Fujinaga M, Kikuchi T, Zhang MR. Development of an in vivo method to estimate effective drug doses and quantify fatty acid amide

hydrolase in rodent brain using positron emission tomography tracer [^{11}C]DFMC. J Pharmacol Exp Ther. 2020;373(3):353–360.

19. Yanamoto K, Yamasaki T, Kumata K, Yui J, Odawara K, Hatori A, Inoue O, Yamaguchi M, Suzuki K, Zhang MR. Evaluation of N-benzyl-N-[11C]methyl-2- (7-methyl-8-oxo-2-phenyl-7,8-dihydro-9H-purin-9-yl)acetamide ([11C]DAC) as a novel translocator protein (18 kDa) radioligand in kainic acid-lesioned rat. Synapse. 2009;63(11):961–971.
20. Yu Z, Jiang N, Su W, Zhuo Y. Necroptosis: a novel pathway in neuroinflammation. Front Pharmacol. 2021;doi: 10.3389/fphar.2021.701564
21. Yuan J, Amin P, Ofengeim D. Necroptosis and RIPK1-mediated neuroinflammation in CNS diseases. Nat Rev Neurosci. 2019;20(1):19–33.
22. Zhang D, Lin J, Han J. Receptor-interacting protein (RIP) kinase family. Cell Mol Immunol. 2010;7(4):243–249.
23. Zhang Y, Chen X, Gueydan C, Han J. Plasma membrane changes during programmed cell deaths. Cell Res. 2018a;28(1):9–21.
24. Zhang X, Ma H, Zheng J, He S. Heteroaryl compounds as inhibitors of necrosis, composition and application thereof. PCT Int. Appl. 2018b;WO 2018017435A1.

Scheme

Scheme 1 and 2 are available in the Supplemental Files Section.

Figures

Figure 1

Chemical structures of receptor-interacting protein 1 kinase (RIPK1) inhibitors.

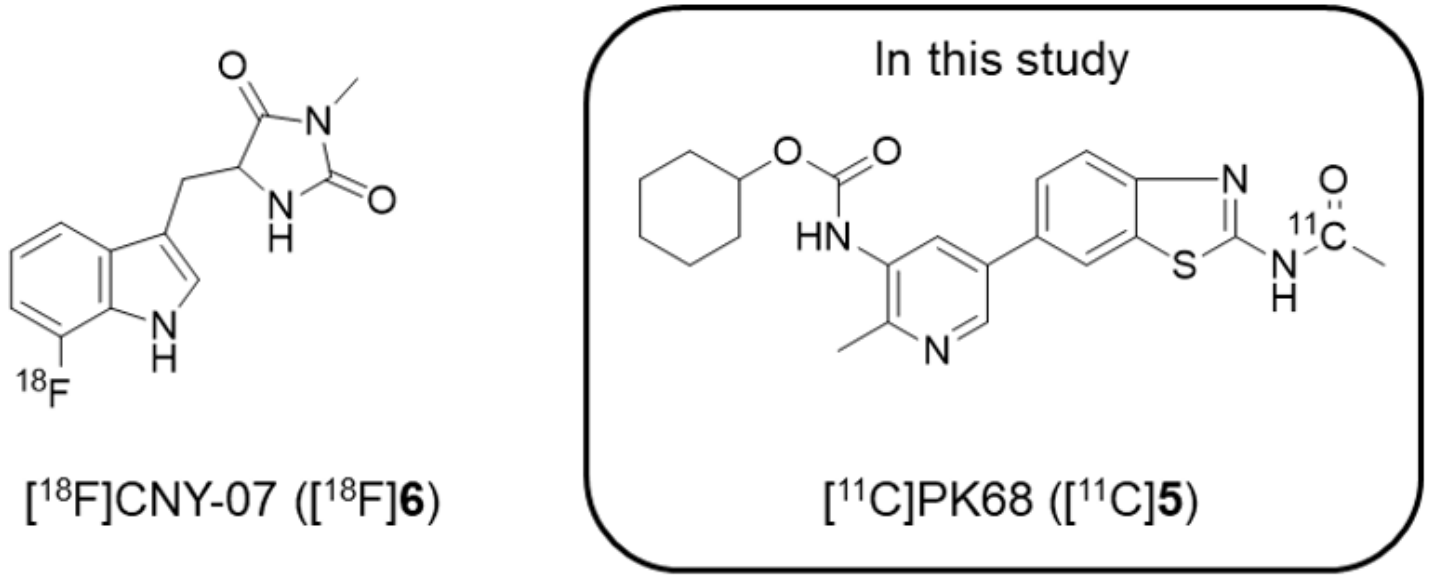

Figure 2

Chemical structures of current radioligands for imaging receptor-interacting protein 1 kinase (RIPK1).

Figure 3

Representative dynamic (0–5, 5–15, 15–30, and 30–60 min) and summed (0–60 min) positron emission tomography (PET) images of [^{11}C]PK68 in mice treated without (baseline, n = 2, A) or with unlabeled PK68 (1 mg/kg, i.v., n = 2, B). Radioactivity in PET images expressed as standardized uptake values (SUVs).

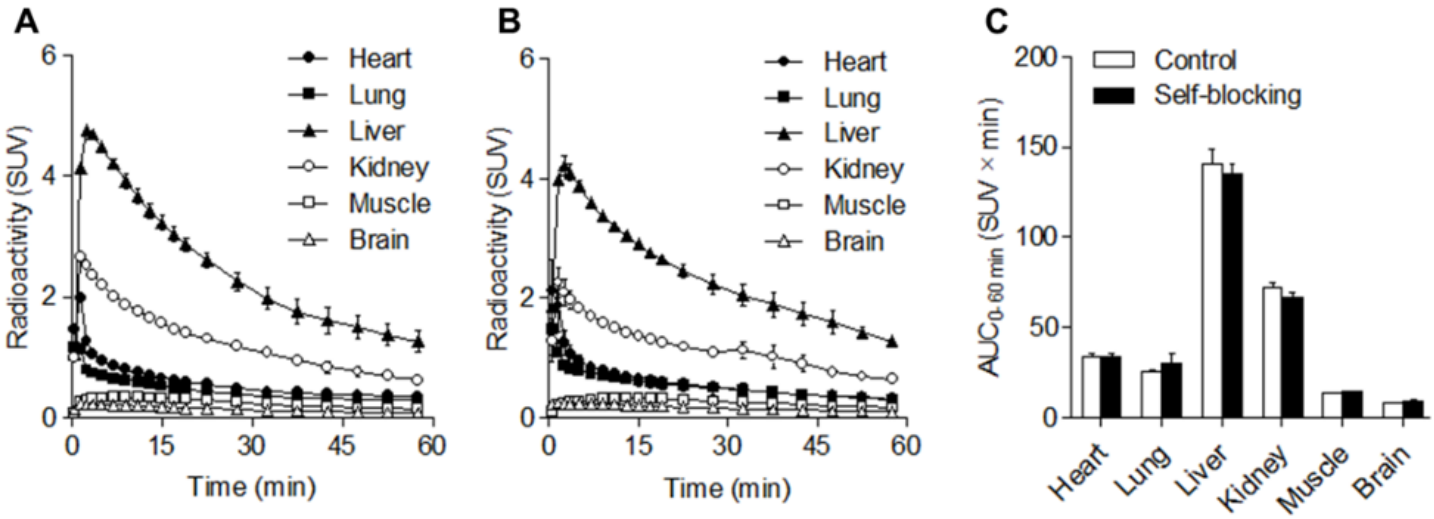

Figure 4

Time–activity curves (n = 2, in each group) of [^{11}C]PK68 in the heart (buried circles), lungs (buried squares), liver (buried triangles), kidneys (open circles), muscle (open squares), and brain (open triangles) of mice treated without (A) or with unlabeled PK68 (1 mg/kg, i.v., B) and areas under the curves (C) in these tissues. Radioactivity is expressed as standardized uptake values (SUVs).

Figure 5

Unchanged form of [^{11}C]PK68 in the plasma and liver of a mouse at 5, 15, 30, and 60 min after injection (n = 2).

Supplementary Files

This is a list of supplementary files associated with this preprint. Click to download.

- Scheme1.png
- Scheme2.png